GEOPHYSICS, VOL. 85, NO. 6 (NOVEMBER-DECEMBER 2020); P. R553–R563, 17 FIGS., 2 TABLES.
10.1190/GEO2019-0816.1

Full-waveform inversion with borehole constraints for elastic VTI media

Sagar Singh[1], Ilya Tsvankin[1], and Ehsan Zabihi Naeini[2]

ABSTRACT

The nonlinearity of full-waveform inversion (FWI) and parameter trade-offs can prevent convergence toward the actual model, especially for elastic anisotropic media. The problems with parameter updating become particularly severe if ultra-low-frequency seismic data are unavailable, and the initial model is not sufficiently accurate. We introduce a robust way to constrain the inversion workflow using borehole information obtained from well logs. These constraints are included in the form of rock-physics relationships for different geologic facies (e.g., shale, sand, salt, and limestone). We develop a multiscale FWI algorithm for transversely isotropic media with a vertical symmetry axis (VTI media) that incorporates facies information through a regularization term in the objective function. That term is updated during the inversion by using the models obtained at the previous inversion stage. To account for lateral heterogeneity between sparse borehole locations, we use an image-guided smoothing algorithm. Numerical testing for structurally complex anisotropic media demonstrates that the facies-based constraints may ensure the convergence of the objective function towards the global minimum in the absence of ultra-low-frequency data and for simple (even 1D) initial models. We test the algorithm on clean data and on surface records contaminated by Gaussian noise. The algorithm also produces a high-resolution facies model, which should be instrumental in reservoir characterization.

INTRODUCTION

Full-waveform inversion (FWI) has been successfully applied to isotropic and anisotropic acoustic media (Tarantola, 1984; Virieux and Operto, 2009; Biondi and Almomin, 2014; Wang and Tsvankin, 2018). However, extension of FWI to more realistic elastic (especially anisotropic) models without properly constraining the inversion entails serious complications, such as trade-offs between the model parameters (Plessix and Cao, 2011; Kamath and Tsvankin, 2016; Wu and Alkhalifah, 2016) and significantly increased computational cost. The advent of computational technology makes application of FWI to such models feasible (Warner et al., 2013; Kamath et al., 2017a; Marjanović et al., 2018), but parameter trade-offs and the resulting loss of spatial resolution impair the inversion results (Kamath and Tsvankin, 2016; Pan et al., 2020). In addition, ultra-low frequencies required by FWI to avoid cycle skipping and improve convergence can seldom be recorded in surface seismic surveys.

Hence, elastic FWI often fails if the initial model does not lie in the "basin of convergence" near the global minimum of the objective function. Multicomponent data generally improve the resolution of the model parameters, especially for anisotropic media (Singh et al., 2018, 2019). However, the signal-to-noise ratio (S/N) on the horizontal displacement components is often too low for their inclusion in FWI.

Therefore, it is essential to use the optimal model parameterization for the problem at hand (Kamath et al., 2017a). Parameter trade-offs can also be reduced by Newton-based optimization methods that use the inverse Hessian matrix (Operto et al., 2013; Pan et al., 2016). Such techniques, however, are computationally expensive and could be ineffective in multiparameter anisotropic FWI, which is typically characterized by a highly multimodal objective function.

Among common approaches to stabilize parameter updating are regularization of the inversion procedure and preconditioning of the inversion gradient (Tikhonov and Arsenin, 1977; Loris et al., 2010; Guitton, 2011; Alkhalifah et al., 2018). These techniques speed up the convergence of model updating, but they require an accurate initial model, and the regularized objective function has to operate with smoothed input data.

Recently, it has been proposed to use so-called optimal transport objective functions to mitigate cycle skipping in FWI (Métivier et al., 2018; Sun and Alkhalifah, 2019). Such methods increase

Manuscript received by the Editor 18 December 2019; revised manuscript received 12 July 2020; published ahead of production 12 August 2020; published online 23 November 2020.
[1]Colorado School of Mines, Center for Wave Phenomena, Golden, Colorado 80401, USA. E-mail: sagarsingh@mymail.mines.edu (corresponding author); ilya@mines.edu.
[2]Earth Science Analytics, London KT3 5HF, UK. E-mail: ehsanzabihi@yahoo.com.

DOI:10.1190/geo2019-0816.1

the convexity of the objective function even in the presence of significant time shifts between the recorded and modeled data. However, the optimal-transport approach usually relies on a highly accurate initial model to resolve the deeper part of the section. In addition, the significant computational cost of this methodology makes its application problematic for 3D field data sets. Wave-equation-based migration velocity analysis is another method that could be effective in improving the accuracy of the velocity model and, therefore, suppressing cycle skipping in FWI (Sun and Alkhalifah, 2018; Li et al., 2019a, 2019b).

The accuracy and spatial resolution of FWI can be increased by incorporating prior information about the subsurface as a constraint in model updating (Guitton et al., 2012; Asnaashari et al., 2013). Whereas such prior information can be obtained from well logs, the sparseness of borehole locations makes it difficult to account for realistic lateral heterogeneity. Kemper and Gunning (2014) and Zabihi Naeini and Exley (2017) propose a framework for amplitude-variation-with-offset (AVO) analysis which uses rock-physics relationships for each facies to increase the accuracy of parameter estimation. A similar methodology for FWI, presented by Kamath et al. (2017b) and Zhang et al. (2018), has produced promising results (Zhang et al., 2017; Singh et al., 2018). However, because Kamath et al. (2017b) incorporate information from a single borehole, an incorrect facies can be assigned to certain grid points for structurally complicated models with pronounced lateral gradients. The same issue leads to artifacts (e.g., edge distortions) in the inversion results of Zhang et al. (2017, 2018).

Singh et al. (2018) propose an image-guided interpolation technique to build a prior confidence model that accounts for lateral heterogeneity. A Bayesian framework is then used to update that confidence model at each iteration. The results of Singh et al. (2018) show that facies-based constraints can guide FWI towards the global minimum, even if the initial model is substantially distorted.

Further improvement in the resolution of elastic FWI can be achieved by incorporating constraints that include all available facies. These facies (e.g., shale, sand, limestone, salt, etc.) can be identified at borehole locations from rock-physics relationships for the elastic parameters. The spatial distribution of these constraints can be built by image-guided interpolation that accounts for lateral heterogeneity (Zabihi Naeini and Hale, 2015). Although facies-based constraints are obtained from prior facies information, they can be updated using the inverted model parameters.

Here, we develop a multiscale FWI algorithm for VTI media that includes facies information as a regularization term in the objective function. That term is updated during the inversion by evaluating the models obtained at the previous inversion stage. The estimates of the spatial facies distribution typically improve as the inversion progresses, which results in more accurate model constraints.

We start by discussing the conventional FWI workflow for elastic VTI media and the main issues that can cause deterioration of the inversion results. Then we outline an efficient approach to constructing facies-based model constraints from available rock-physics relationships. The algorithm is applied to the 2D VTI Marmousi model with two different initial parameter fields that provide a good approximation for the reflection traveltimes. We carry out the inversion using geophone (multicomponent) data as well as hydrophone (pressure) recordings. Comparison with conventional (unconstrained) FWI demonstrates the benefits of facies-based constraints in suppressing the inversion nonlinearity and increasing parameter resolution.

WAVEFORM INVERSION FOR VTI MEDIA

Conventional FWI algorithms use the least-squares objective function $E_{\mathrm{d}}(\mathbf{m})$ to minimize the misfit between the simulated and observed seismic data:

$$E_{\mathrm{d}}(\mathbf{m}) = ||\mathbf{W}_{\mathrm{d}}(\mathbf{d}^{\mathrm{sim}} - \mathbf{d}^{\mathrm{obs}})||^2, \tag{1}$$

where $\mathbf{d}^{\mathrm{obs}}$ denotes the recorded data, $\mathbf{d}^{\mathrm{sim}}$ is the data simulated for a certain trial model, and $\mathbf{W}_{\mathrm{d}}$ is a data-weighting operator designed to make the objective function dimensionless.

Multiparameter models generally make the inverse problem more nonlinear and may increase the number of local minima of the objective function. In that case, the initial model has to lie in the immediate vicinity (basin of convergence) of the global minimum. Then the inversion can be implemented via an efficient local gradient-based approach:

$$\mathbf{m}_{i+1} = \mathbf{m}_i + \alpha_i \mathbf{P}_i, \tag{2}$$

where $\mathbf{m}_i$ is the model-parameter vector at the ith iteration, α_i is the step length, and $\mathbf{P}_i$ is the direction of the model updating. Below we supplement the conventional objective function in equation 1 with facies-based constraints.

To model seismic data for VTI media, we use the elastic wave equation:

$$\rho \frac{\partial^2 u_i}{\partial t^2} = \frac{\partial}{\partial x_j}\left[c_{ijkl}\frac{\partial u_k}{\partial x_l}\right] + F_i, \tag{3}$$

where $\mathbf{u}$ is the displacement field, ρ is the density, $\mathbf{F}$ is the body force per unit volume, and $c_{\mathrm{ijkl}}(i,j,k,l = 1,2,3)$ are the stiffness coefficients; summation over repeated indices is implied. The pressure data can be simulated by summation of the diagonal components of the stress tensor. The gradient of the objective function with respect to the model parameters is computed from the adjoint-state method (Kamath and Tsvankin, 2016):

$$\frac{\partial E_{\mathrm{d}}(\mathbf{m})}{\partial \mathbf{m}} = -\left[\frac{\partial \mathbf{d}^{\mathrm{sim}}}{\partial \mathbf{m}}\right]^T \mathbf{W}_{\mathrm{d}}^T \mathbf{W}_{\mathrm{d}}(\mathbf{d}^{\mathrm{obs}} - \mathbf{d}^{\mathrm{sim}}), \tag{4}$$

where the subscript "T" denotes the transpose.

The relationships between the stiffness coefficients and VTI parameters, as well as the exact expressions for the FWI gradient can be found in Appendix A. For the numerical examples below, iterative parameter updating is carried out with a multiscale approach using the nonlinear conjugate-gradient algorithm (Hager and Zhang, 2006).

FACIES-BASED CONSTRAINTS AS A REGULARIZATION TERM

We supplement the conventional data-fitting objective function $E_{\mathrm{d}}(\mathbf{m})$ in equation 1 with facies-based constraints as follows:

$$E(\mathbf{m}) = E_{\mathrm{d}}(\mathbf{m}) + \beta E_f(\mathbf{m}), \tag{5}$$

$$E_f(\mathbf{m}) = ||\mathbf{W}_m(\mathbf{m}^{\mathrm{inv}} - \mathbf{m}^{\mathrm{f}})||^2. \tag{6}$$

Here, the vector $\mathbf{m}^{\mathrm{f}}$ represents the facies-based constraints, $\mathbf{m}^{\mathrm{inv}}$ is the inverted model, β is a scaling factor, and $\mathbf{W}_{\mathrm{m}}$ is a diagonal scaling matrix designed to make the facies-based term dimensionless and to assign larger weights to data around borehole locations, where accurate lithologic information is available. The gradient of the objective function in equation 5 can be found as follows:

$$\frac{\partial E(\mathbf{m})}{\partial \mathbf{m}} = -\left[\frac{\partial \mathbf{d}^{\mathrm{sim}}}{\partial \mathbf{m}}\right] \mathbf{W}_{\mathrm{d}}^{T}\mathbf{W}_{\mathrm{d}}\,(\mathbf{d}^{\mathrm{obs}} - \mathbf{d}^{\mathrm{sim}}) + \beta \mathbf{W}_{\mathrm{m}}^{T}\mathbf{W}_{\mathrm{m}}(\mathbf{m}^{\mathrm{inv}} - \mathbf{m}^{\mathrm{f}}), \tag{7}$$

where the second term on the right-hand side of equation 7 corresponds to the derivative of equation 6 with respect to the model vector.

The prior rock-physics constraints in the term $\mathrm{E}_f(\mathbf{m})$ are supposed to be based on the identified geologic facies, which are typically determined by an interpreter using indirect measurements (e.g., well logs). The facies-based term is similar to that in Singh et al. (2018), where the initial constraints are obtained from image-guided interpolation (Zabihi Naeini and Hale, 2015). After identifying facies at the available borehole locations, the borehole data are used to determine the elastic properties for each facies (herein referred to as "depth trends").

Interpolation or extrapolation of sparse well-log data may not properly account for substantial lateral heterogeneity. The realizations (f_{realize}) of different lithologic facies (such as shale, sand, and lime) are obtained by using the facies relationships (p) combined with the model ($\mathbf{m}$) computed by image-guided interpolation:

$$f^{x}_{\mathrm{realize}} = \mathcal{F}(\mathbf{m})|_{p_x}, \tag{8}$$

where x is the facies number, which ranges from one to N (N corresponds to the total number of identified facies), and $\mathcal{F}$ is a function that generates the elastic model by applying the identified facies relationships p.

The facies classification is based on the realization that provides the best match with the grid-point (i, j) value in the interpolated model:

$$\mathrm{facies}(i,j) := \min_{x=1,2\ldots N}\{f^{x}_{\mathrm{realize}}(i,j) - m(i,j)\}. \tag{9}$$

Equation 9 produces an integer between 1 and N that identifies the facies present at a certain grid point. Then, the best-matched elastic property (m_f) is assigned using the depth trends (D_T) for that facies:

$$m_f(i,j) := \min_{n=1\ldots k}\{m_{\mathrm{inv}}(i,j) - D_T(n)|_{\mathrm{facies}(i,j)}\}, \tag{10}$$

where k is total number of the parameter values in D_T that corresponds to a certain facies.

Because the constraints depend on the parameters estimated at each inversion stage along with the facies identified in the well logs, the facies-based updates are influenced by the inversion results. Therefore, we refer to these constraints as "facies-based models." Hence, the FWI workflow is constrained by the rock-physics relationships for each individual facies. In addition to the estimated parameters ($\mathbf{m}^{\mathrm{inv}}$), the algorithm produces the final facies-based models ($\mathbf{m}^{\mathrm{f}}$), which could be efficiently used in reservoir characterization.

SYNTHETIC TEST ON VTI MARMOUSI MODEL

We test the proposed methodology on the modified 2D elastic VTI Marmousi model (Martin et al., 2006). The elastic wave equation 3 is solved using a fourth-order finite-difference algorithm on a staggered grid with convolutional perfectly matched layers (CPML) boundary conditions on the sides of the model and a free surface on top. The medium is parameterized by the P- and S-wave vertical velocities (V_{P0} and V_{S0}) and the P-wave horizontal and normal-moveout (NMO) velocities ($V_{\mathrm{hor,P}}$ and $V_{\mathrm{nmo,P}}$). These four parameters control the signatures of the in-plane polarized P- and SV-waves in VTI media.

The advantages of this parameterization in mitigating the parameter trade-offs are discussed by Kamath et al. (2017a). In addition, all parameters have the same units and, typically, a similar spatial structure. Therefore, a single migrated section can be used for image-guided interpolation. In addition, the inversion gradients for all parameters are expected to have comparable magnitudes. The horizontal and NMO velocities can be expressed through the Thomsen parameters ϵ and δ as (Tsvankin, 2012):

$$V_{\mathrm{hor,P}} = V_{\mathrm{P0}}\sqrt{1+2\epsilon},$$
$$V_{\mathrm{nmo,P}} = V_{\mathrm{P0}}\sqrt{1+2\delta}. \tag{11}$$

For our version of the Marmousi model, we define the anisotropy coefficients through the density as follows: $\epsilon = 0.25\rho - 0.3$ and $\delta = 0.125\rho - 0.1$ (Duan and Sava, 2016). (Note that in general, the density and anisotropy coefficients may not be related. The anisotropy parameters can potentially serve as additional facies indicators for fine tuning the facies classification and rock-physics relationships.) The section is overlaid by a 460 m thick water layer (Figure 1a, 1d, 1g, 1j, and 1m). To illustrate the strength of anisotropy for this model, Figure 2 shows Thomsen's anisotropy coefficients ϵ and δ.

We generate both pressure data that simulate hydrophone recordings and multicomponent data that could be acquired on the seafloor. The wavefield is excited by 116 shots and recorded by 400 receivers evenly distributed along the line and placed 40 and 460 m, respectively, beneath the surface. The receiver locations are the same for both hydrophone and geophone data. The source represents a point explosion; the source signal is a Ricker wavelet with a central frequency of 10 Hz.

The source wavelet and recorded data are filtered (using the selected frequency range, see below) prior to the inversion. To improve the convergence of the optimization method and avoid local minima of the objective function, the amplitude decay with depth due to geometric spreading and multiple reflections in the overburden needs to be compensated for. We precondition the gradients using the inverse Hessian matrix, which is obtained by the zero-lag correlation of the magnitude of the forward wavefield with an approximate receiver Green's function (Plessix and Mulder, 2004). This procedure eliminates the need for additional data weighting, so each element of $\mathbf{W}_{\mathrm{d}}$ in equation 1 is set to unity (note that the units of $\mathbf{W}_{\mathrm{d}}$ are 1/dim($\mathbf{d}$)). The algorithm is designed to estimate all five pertinent medium parameters (V_{P0}, V_{S0}, $V_{\mathrm{hor,P}}$, $V_{\mathrm{nmo,P}}$, and ρ) simultaneously using the inversion gradients listed in Appendix A. The low frequencies in the 0–2 Hz range, which can seldom be acquired in the field, are filtered out from the observed data.

Inversion with 1D initial model

First, we use a 1D initial model (Figure 1b, 1e, 1h, 1k, and 1n) obtained at one of the borehole locations (x = 1.2 km). Figure 3 displays vertical profiles that illustrate the deviations of the initial parameters from the actual values and the inversion results obtained by conventional FWI and our algorithm.

The output of FWI without facies-based constraints is shown in Figure 4a, 4d, 4g, 4j, and 4m; the inversion was performed for pressure (hydrophone) data from all shots in four frequency bands (2–3, 2–5, 2–10, and 2–20 Hz). Whereas the estimates of the vertical velocities (V_{P0} and V_{S0}) and the P-wave horizontal velocity ($V_{hor,P}$) are sufficiently accurate at least in the upper part of the section (z < 1.5 km), the P-wave NMO velocity and density are strongly distorted even up shallow. The errors in the model parameters increase with depth due to the absence of low frequencies, inaccurate initial model, and parameter trade-offs (Figure 3). For example, on the left side (x < 3 km) of the section, the reflector positions are inaccurate, and the shape of the salt intrusion is distorted (2.8 < z < 3.2 km).

To determine whether the addition of facies information can overcome these problems, we apply our FWI algorithm using the multiscale approach with the same frequency bands. The rock-physics constraints for the inversion workflow are computed from borehole data at two locations (Figure 5). Here, we assume that the borehole information is available only down to a certain depth. To obtain the facies distribution, we use the rock-physics relationships between V_{P0} and V_{S0} and also between V_{P0} and ρ for the original isotropic Marmousi model (Table 1). The crossplot of these relationships (Figure 6) confirms that the correlation between V_{P0} and ρ for this model is more reliable because different facies can be easily picked and then used for constraining the inversion.

After extracting the part of the well-log data corresponding to a particular facies (Figure 7), we compute the distribution of that facies between the boreholes. Although the accuracy of facies determination would increase if more well logs were available, even sparse prior information improves the convergence of FWI. The

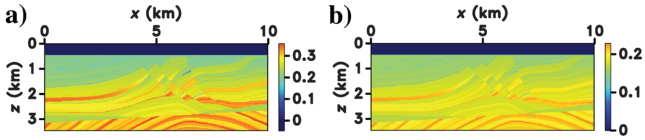

Figure 2. Thomsen's anisotropy coefficients of the Marmousi model: (a) ϵ and (b) δ.

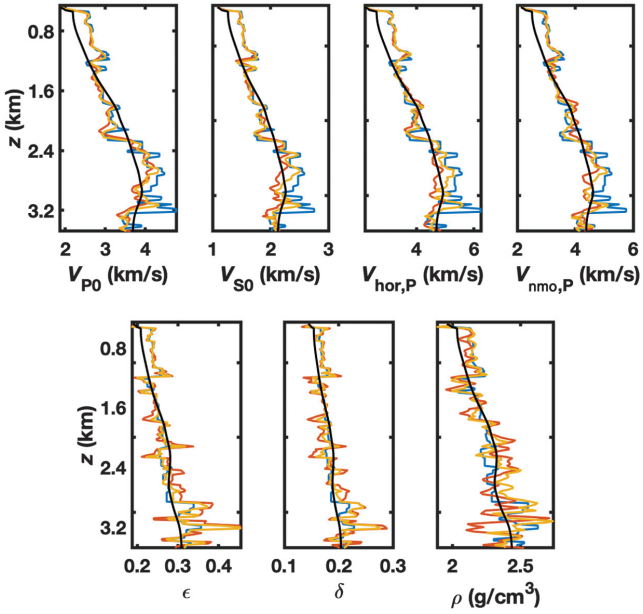

Figure 3. Vertical profiles of the VTI parameters at x = 6 km. The actual parameters are marked by the blue lines, and the corresponding initial parameters (the initial model is 1D) used for FWI are in black. The red and yellow lines mark the inversion results for the pressure data obtained by the unconstrained and facies-based FWI, respectively.

Figure 1. Parameters of the VTI Marmousi model: (a) the P-wave vertical velocity (V_{P0}), (d) the S-wave vertical velocity (V_{S0}), (g) the P-wave horizontal velocity ($V_{hor,P}$), (j) the P-wave normal-moveout velocity ($V_{nmo,P}$), and (m) the density (ρ). The corresponding 1D initial models of (b) V_{P0}, (e) V_{S0}, (h) $V_{hor,P}$, (k) $V_{nmo,P}$, and (n) ρ and 2D smoothed initial models of (c) V_{P0}, (f) V_{S0}, (i) $V_{hor,P}$, (l) $V_{nmo,P}$, and (o) ρ.

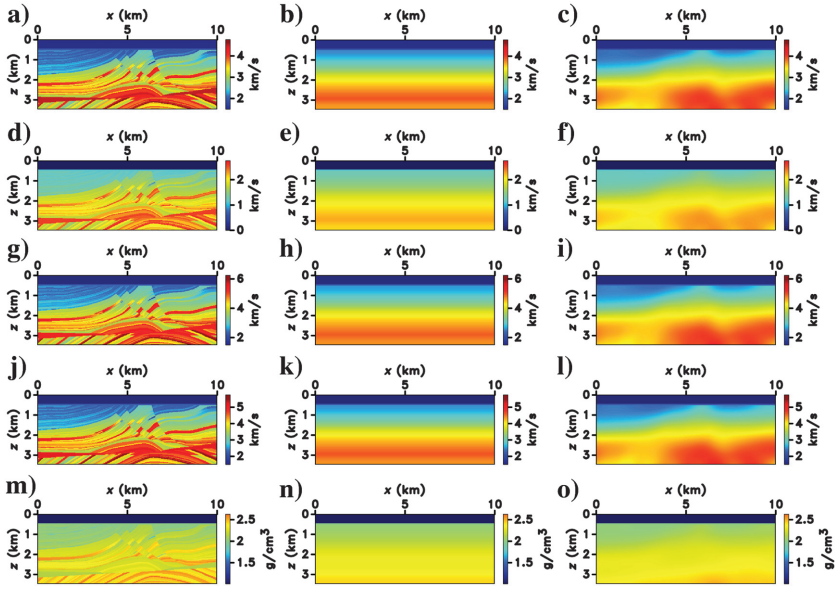

initial facies-based constraints are computed by interpolating the values obtained at the borehole locations along a migrated image of the inversion gradient (Figure 8a). Our facies-based FWI algorithm is implemented as follows:

1) Compute the elastic properties at the borehole locations for each facies based on the available rock-physics relationships (Table 1).
2) Interpolate the obtained borehole data using a migrated image.
3) Use the $[V_{P0}, \rho]$ crossplot to generate different realizations of the density ρ from the velocity V_{P0} for such facies as shale, sand, and lime. The facies relationships in the $[V_{P0},V_{S0}]$ domain exhibit more overlap which makes the classification more difficult. In practice, one can use a combination of different elastic parameters depending on the available borehole data.
4) Classify facies for the entire section by finding the best-matched realization at each grid point of the current model. This classification is based on the minimum distance between a value of the inverted parameter (or the parameter determined from image-guided interpolation for the first inversion stage) at each grid point and the corresponding realization value.
5) After the facies region has been classified, go back to step 1 to assign the best-matching elastic property at each grid point for the modeled facies.
6) Repeat the entire process for the next inversion stage.

In the current implementation of the algorithm, we do not apply facies-based constraints until reaching "intermediate" frequencies (approximately 10 Hz). Numerical testing shows that the interpolated models generated at step 2 are sufficient to constrain the inversion for lower frequencies.

As mentioned above, the matrix $\mathbf{W}_m$ is designed to assign larger weights to the data at the borehole locations (equation 6). To be consistent with the gradient preconditioning applied to the data-fitting term (E_d), we apply a correction for geometric spreading to the function E_f (Figure 9). This approach is similar to that in Asnaashari et al. (2013), where the operator $\mathbf{W}_m^T\mathbf{W}_m$ is scaled by $1/z^2$, where z is the depth (note that the amplitude decay due to geometric spreading approximately is inversely proportional to z). The data at depths

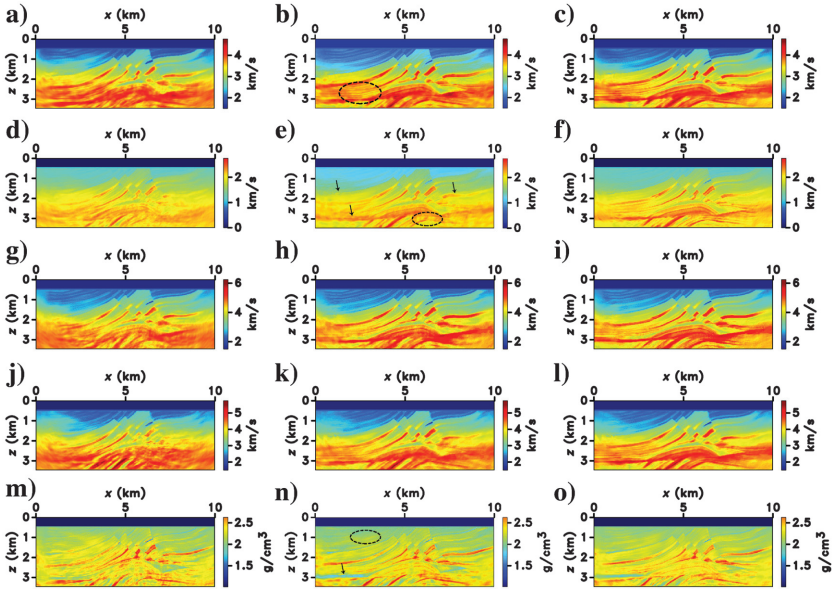

Figure 4. Results of the conventional FWI of the pressure data using the 1D initial model in Figures 1 and 2: (a) V_{P0}, (d) V_{S0}, (g) $V_{hor,P}$, (j) $V_{nmo,P}$, and (m) ρ. The corresponding results of the facies-based FWI: (b) V_{P0}, (e) V_{S0}, (h) $V_{hor,P}$, (k) $V_{nmo,P}$, and (n) ρ. The results of the facies-based FWI using the multicomponent data: (c) V_{P0}, (f) V_{S0}, (i) $V_{hor,P}$, (l) $V_{nmo,P}$, and (o) ρ. The frequency range for the inversion is 2–20 Hz. Areas of major improvements achieved by the facies-based FWI are marked by ellipses.

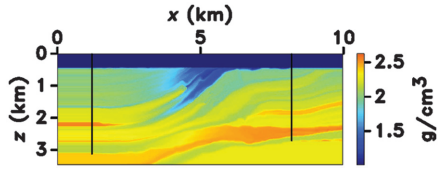

Figure 5. Interpolated density model obtained using borehole data at the two locations marked by the vertical lines (x = 1.2 km and 8.4 km).

Table 1. Isotropic rock-physics relationships for each facies in the Marmousi model (adapted from Martin et al., 2006).

Facies relationships

Facies (f)	V_P (m/s)	V_S (m/s)	ρ (g/cm^3)
Water	1500	0	1.01
Sand	V_P	$V_S = 0.804V_P - 856$	$\rho = 0.2736V_P^{0.261}$
Shale	V_P	$V_S = 0.770V_P - 867$	$\rho = 0.2806V_P^{0.265}$
Marl	V_P	$V_S = 1.017 * 10^{-3}V_P - 0.055 * 10^{-6}V_P^2 - 1.03$	$\rho = 0.3170V_P^{0.225}$
Salt	4500	2600	2.14

Note: The spatially varying P-wave velocity is denoted by V_P (same as V_{P0} in Figure 1a).

for which there is no borehole information are assigned lower weights.

The facies-based term in equation 3 is scaled by the factor β. At each iteration, β can be adjusted to improve the convergence toward the actual model. Such adjustment for field-data applications should depend on the accuracy of the prior model and data quality.

The facies-based method reconstructs the model parameters with a higher accuracy (Figure 4b, 4e, 4h, 4k, and 4n) than the conventional FWI (also see Figure 3). We observe further improvement in the inversion results if multicomponent data (rather than pressure) are used (Figure 4c, 4f, 4i, 4l, and 4o). In particular, note the increased spatial resolution of the gradient image (Figure 8b).

The density, which is often poorly constrained by surface seismic data, is accurately estimated only down to 2.4 km. The quality of density reconstruction decreases between 2.4 and 3.0 km; however, the inverted density becomes more accurate below 3 km (Figure 3). The final facies-based constraints (Figure 10) closely match the actual models, which means that the inversion was properly constrained. It is clear that the employed lithologic constraints efficiently guide the inversion toward the global minimum of the objective function (Figure 11).

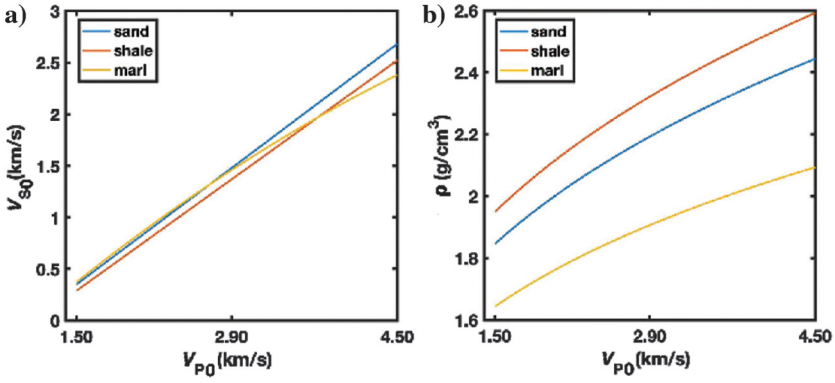

Figure 6. Facies relationships at the borehole locations. The crossplots of (a) [V_{P0}, V_{S0}] and (b) [V_{P0}, ρ]. The [V_{P0}, ρ] crossplot is used to assign the facies at each grid point because the curves for different facies on plot (b) dot not overlap.

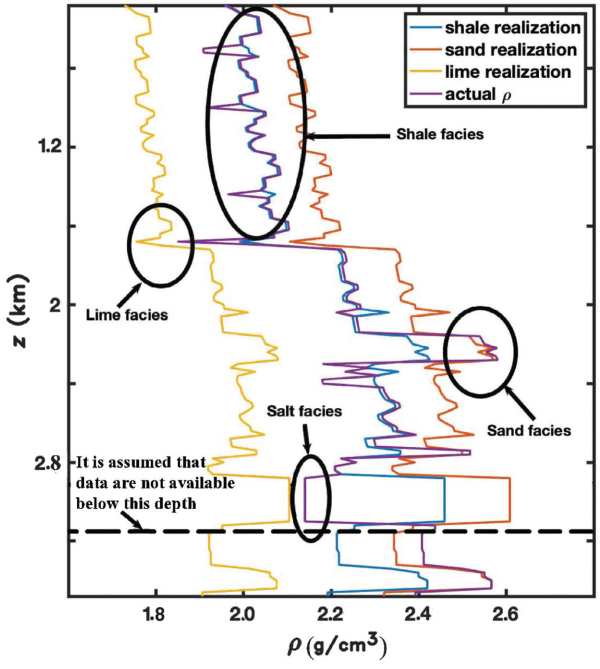

Figure 7. Depth trends at x = 1.2 km. The facies relationships are used to separate the density curve into the depth intervals of different facies.

FWI with 2D initial model

The 1D initial model used above does not include the high-wavenumber components of the actual model. Although the facies-based constraints increase the resolution of the medium parameters, an additional improvement can be achieved with a more accurate initial model. Next, we obtain the initial model (Figure 1c, 1f, 1i, 1l, and 1o) by applying Gaussian-based smoothing (with the standard deviation of the Gaussian kernel set to 20) to the actual parameter distributions. Presumably, a similar 2D initial model can be obtained by reflection tomography (Xu et al., 2012; Wang and Tsvankin, 2013) or other postmigration velocity-analysis methods.

As before, FWI is first carried out for the pressure data from all shots in the same four frequency bands without facies-based constraints. The higher accuracy of the initial model improves the results of the conventional FWI (Figure 12a, 12d, 12g, 12i, and 12m). Nonetheless, most reflectors are still mispositioned, and the spatial resolution in the deeper part of the section is low. In particular, the NMO velocity is the least resolved parameter in the inversion that suffers the most from the parameter trade-offs. Furthermore, the S-wave vertical velocity V_{S0} is not well recovered from the pressure data, especially inside the salt intrusion. Similar problems can be seen in the V_{S0}-field obtained using the 1D initial model (Figure 4d).

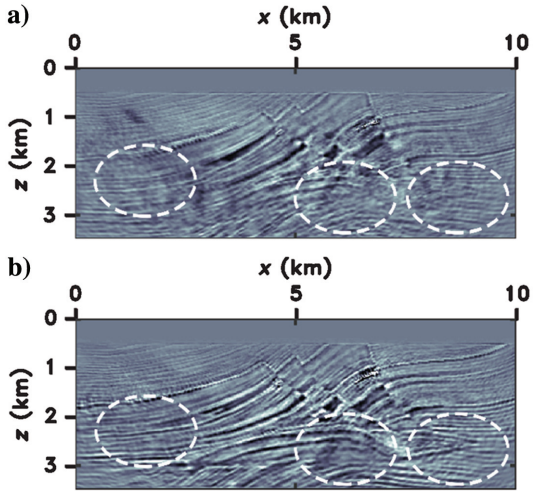

Figure 8. Inversion gradient for the velocity V_{P0} obtained for the final model using (a) the conventional FWI and (b) the facies-based FWI. The improvements achieved by the facies-based FWI are marked by the ellipses.

Next, we regularize FWI with the facies-based constraints described in the previous section. Our method succeeded in resolving the model parameters with a much higher accuracy (Figure 12b, 12e, 12h, 12k, and 12n) than the unconstrained FWI. Note that the inverted velocity V_{S0} accurately delineates the salt intrusion. The constraints help reconstruct the P-wave NMO velocity with a similar resolution and accuracy as the other parameters, even in the deeper part of the section. The density, poorly estimated by the unconstrained FWI, is better resolved due to the impact of the facies-based constraints and higher accuracy of the initial density model (Figure 13). Including the multicomponent data in the facies-based FWI (Figure 12c, 12f, 12i, 12l, and 12o) helps constrain the medium parameters at intermediate and large depths. Because of the higher sensitivity of the multicomponent data to S-waves, the spatial resolution of V_{S0} is noticeably increased. Most structural features, especially the salt intrusion, become recognizable in the V_{S0}-field.

Although the inclusion of the multicomponent data increases the parameter resolution, the facies-based FWI of the pressure data adequately reconstructs most parameter fields, especially the velocities $V_{nmo,P}$, and $V_{hor,P}$ and density (but not the salt intrusion in the V_{S0} field; Figure 12). Figure 14 confirms that the prior facies information helps guide the updating algorithm towards the global minimum of the objective function.

FWI of noisy data

To test the robustness of the algorithm, we contaminate the input pressure data with noise using a pseudorandom Gaussian function. The S/N ratio is set to 15, which corresponds to the typical noise level in marine seismic data (Figure 15).

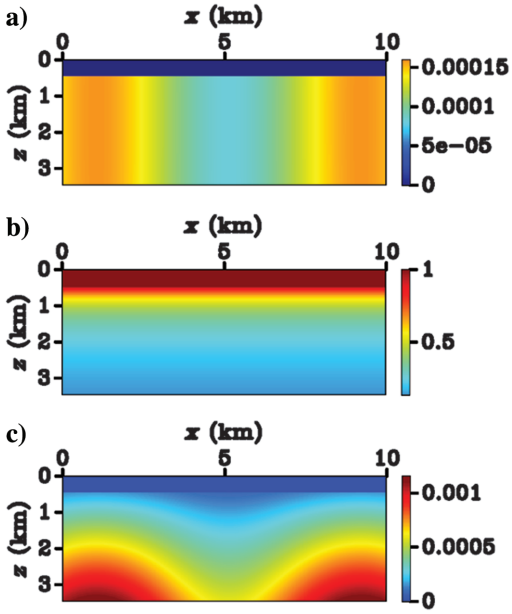

Figure 9. Diagonal elements of the model-weighting matrix $\mathbf{W}_m$ used for the inversion. (a) The Gaussian function that varies only in the x-direction between two boreholes with the maximum value assigned near the borehole locations; (b) the function that compensates for amplitude decay due to geometric spreading, and (c) the weighting parameter obtained by multiplying the function from plot (a) with the inverse of the function from plot (b).

Despite using the 2D initial model, the unconstrained FWI fails to adequately recover the model parameters (Figure 16a, 16c, 16e, 16g, and 16i). Whereas the inversion results for noise-free data are much better (Figure 13), many features of the inverted models obtained from the clean and noisy data are similar. For example, in both cases, the P-wave NMO velocity is the least resolved parameter, and the S-wave velocity V_{S0} is not recovered around the salt intrusion. Figure 17 shows that the influence of noise makes the pressure data less sensitive to the P-wave horizontal velocity. It should be noted that the noise causes deterioration of the inversion results even in the shallow layers.

By adding prior information about the facies, our algorithm mitigates the influence of noise and clearly outperforms the conventional FWI (Figure 16b, 16d, 16f, 16h, and 16j). Still, the deeper part of the section is not as well resolved as for the noise-free data (Figure 17). Indeed, reflections from the deeper interfaces have lower amplitudes and are more strongly distorted by noise. In that case, applying pseudoHessian preconditioning only leads to amplifying the noise.

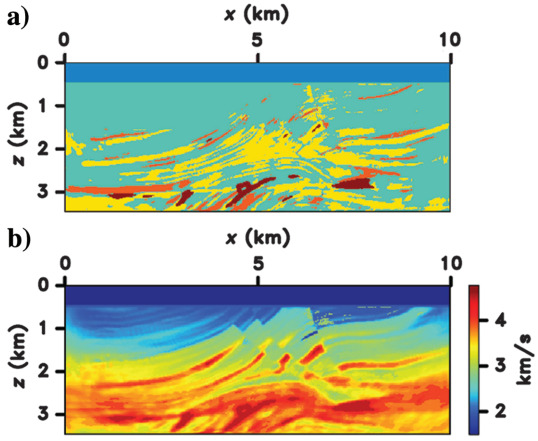

Figure 10. (a) Final facies model produced by the facies-based FWI (water, shale, sand, lime, and salt) and (b) the P-wave vertical velocity V_{P0} obtained by assigning the best-matched elastic property for each facies.

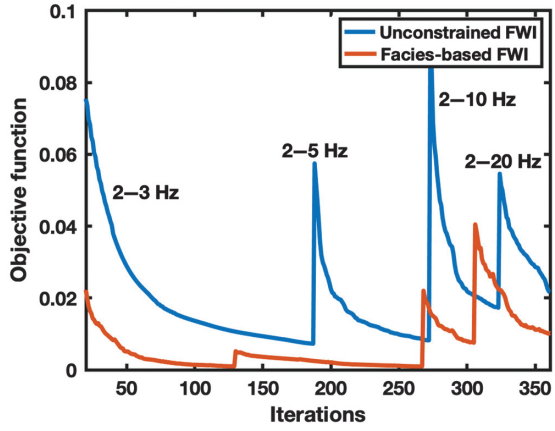

Figure 11. Normalized objective function for different frequency bands. The curve starts with the 20th iteration, which makes the variations for subsequent iterations more visible.

DISCUSSION

Acquisition of marine seismic data is typically performed with hydrophones that record the pressure field. Pressure data, however, are not sufficiently sensitive to some elastic parameters, such as the S-wave vertical velocity V_{S0}. Multicomponent data acquired at the sea floor generally improve the resolution of elastic FWI for anisotropic media and can make it possible to constrain the velocity V_{S0}. However, they also generally make the objective function more multimodal, which hinders the convergence toward the global minimum.

The proposed approach that incorporates prior facies information significantly improves the inversion results even for input hydro-

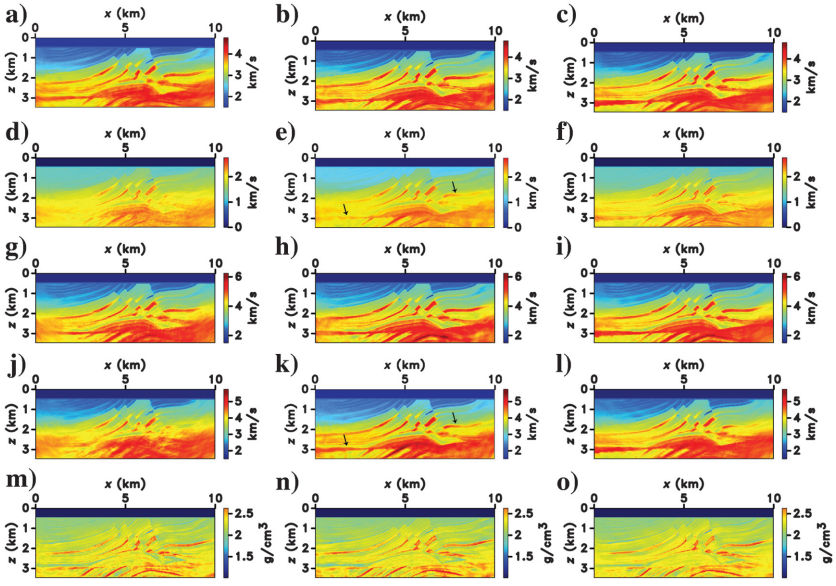

Figure 12. Results of the conventional FWI of the pressure data for the 2D initial model in Figure 1: (a) V_{P0}, (d) V_{S0}, (g) $V_{hor,P}$, (j) $V_{nmo,P}$, and (m) ρ. The corresponding results of the facies-based FWI: (b) V_{P0}, (e) V_{S0}, (h) $V_{hor,P}$, (k) $V_{nmo,P}$, and (n) ρ. The results of the facies-based FWI using multicomponent data: (c) V_{P0}, (f) V_{S0}, (i) $V_{hor,P}$, (l) $V_{nmo,P}$, and (o) ρ. The frequency range for the inversion is 2–20 Hz.

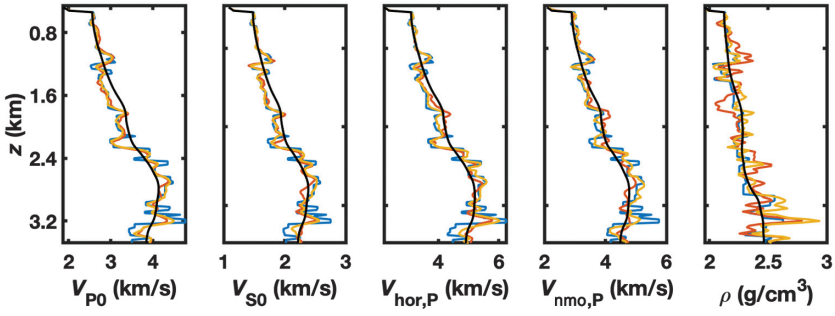

Figure 13. Vertical profiles of the VTI parameters at $x = 6$ km. The actual parameters are marked by the blue lines, and the corresponding initial parameters (the initial model is 2D) used for FWI are in black. The inversion results for the pressure data are marked by the red and yellow lines for the unconstrained and facies-based FWI, respectively.

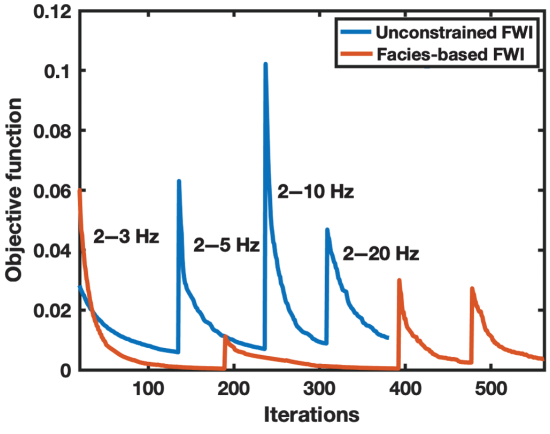

Figure 14. Normalized objective function for different frequency bands.

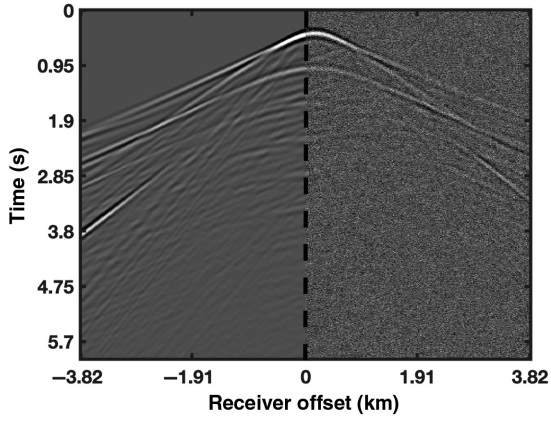

Figure 15. Pressure recording for shot #58 at $x = 5$ km. The panel to left of the dashed line contains clean data and to the right are noise-contaminated data with the signal-to-noise ratio equal to 15.

phone records. Despite often being collected far from the target region, properly weighted borehole data can be included in the inversion algorithm using image-guided interpolation. Borehole data (usually well logs) serve as the primary source of geologic information about the subsurface.

However, the limited number of available boreholes could be problematic for the facies-based FWI and lead to distortions away from the borehole locations. Furthermore, it is difficult to map all subsurface facies just from sparse well-log measurements. Therefore, the accuracy of the facies model tends to decrease away from the boreholes.

Data contamination with noise poses a major challenge to FWI including our algorithm. Despite the satisfactory results obtained for a realistic level of noise (S/N = 15), the inversion may become unreliable, if the S/N decreases to approximately 10. For noisy data, the scaling factor (β) should be adjusted depending on the accuracy of the prior model and noise level.

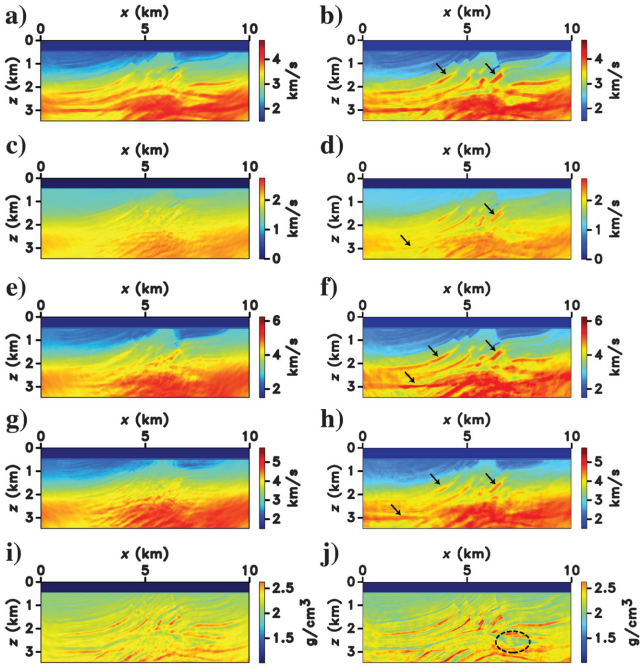

Figure 16. Results of the conventional FWI of the noisy pressure data (see Figure 15) for the 2D initial model in Figure 1: (a) V_{P0}, (d) V_{S0}, (g) $V_{hor,P}$, (j) $V_{nmo,P}$, and (m) ρ. The corresponding results of the facies-based FWI: (b) V_{P0}, (e) V_{S0}, (h) $V_{hor,P}$, (k) $V_{nmo,P}$, and (n) ρ. The frequency range for the inversion is 2–20 Hz.

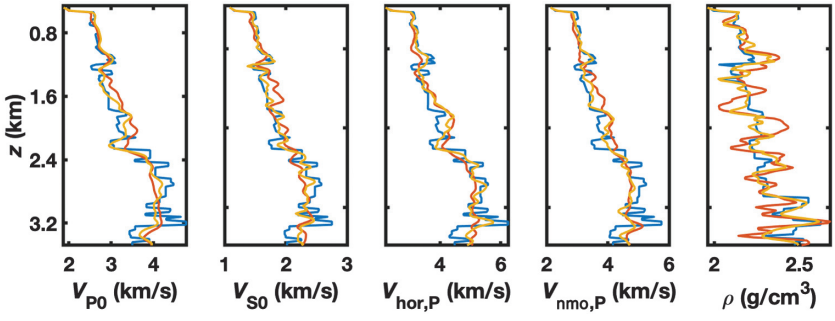

Figure 17. Vertical profiles of the VTI parameters at $x = 6$ km. The actual parameters are marked by the blue lines. The inversion results for the noisy pressure data are marked by the red and yellow lines for the unconstrained and facies-based FWI, respectively.

CONCLUSIONS

We proposed a regularization framework designed to incorporate prior information about the geologic facies into the FWI workflow. The rock-physics descriptions of different facies are supposed to be obtained from the available well logs. Because borehole locations are generally sparse, the spatial distribution of the facies-based constraints at each inversion stage is created by finding the best-matched facies realization for each grid point of the inverted model. Application to the elastic VTI Marmousi model shows that even if the initial model is inaccurate (e.g., 1D) and ultra-low-frequency data are unavailable, these constraints substantially reduce the nonlinearity of FWI and guide the inversion toward the global minimum of the objective function. Although including multicomponent data improves the spatial resolution of the inverted parameters, the facies-based FWI of pressure recordings yields an adequate reconstruction of most parameter fields.

ACKNOWLEDGMENTS

This work was supported by the Consortium Project on Seismic Inverse Methods for Complex Structures at the Center for Wave Phenomena (CWP). We thank Vladimir Li from Ikon Science, UK for his help with 2D image-guided interpolation. We are grateful to the members of the A(anisotropy)-Team at CWP for useful discussions.

DATA AND MATERIALS AVAILABILITY

Data associated with this research are available and can be obtained by contacting the corresponding author.

APPENDIX A

INVERSION GRADIENTS FOR FULL-WAVEFORM INVERSION IN VTI MEDIA

Our algorithm operates with the P- and S-wave vertical velocities (V_{P0} and V_{S0}), P-wave normal-moveout and horizontal velocities ($V_{nmo,P}$ and $V_{hor,P}$), and density (ρ). These parameters control P- and SV-wave propagation in VTI media. The pertinent stiffness coefficients are related to these velocities as follows:

$$C_{11} = \rho V_{hor,P}^2, \tag{A-1}$$

$$C_{13} = \rho\left[\sqrt{(V_{P0}^2 - V_{S0}^2)(V_{NMO,P}^2 - V_{S0}^2)} - V_{S0}^2\right], \tag{A-2}$$

$$C_{33} = \rho V_{P0}^2, \tag{A-3}$$

$$C_{55} = \rho V_{S0}^2. \tag{A-4}$$

The gradient of the FWI data-difference objective function (equation 1) for elastic VTI media is obtained by Kamath and Tsvankin (2016) as

$$\frac{\partial \mathrm{E_d}}{\partial m_n} = -\sum_{ijkl} \frac{\partial c_{ijkl}}{\partial m_n} \left(\int_0^T \frac{\partial u_i}{\partial x_j} \frac{\partial \psi_k}{\partial x_l} \right), \tag{A-5}$$

where T is the total time of wave propagation, $\mathbf{u}$ and $\boldsymbol{\psi}$ are the forward- and back-propagated displacement fields, respectively, and the vector $\mathbf{m}$ includes the model parameters ($m_1 = V_{\mathrm{P0}}$, $m_2 = V_{\mathrm{S0}}$, $m_3 = V_{\mathrm{nmo,P}}$, $m_4 = V_{\mathrm{hor,P}}$, and $m_6 = \rho$); in 2D, $i, j, k, l = 1, 2$.

The derivatives of the objective function with respect to velocity parameters are (Kamath and Tsvankin, 2016)

$$\frac{\partial E_{\mathrm{d}}}{\partial V_{\mathrm{P0}}} = -2\rho V_{\mathrm{P0}} \int_0^T \left[\frac{\partial \psi_z}{\partial z} \frac{\partial u_z}{\partial z} + \frac{q}{2} \left(\frac{\partial \psi_x}{\partial x} \frac{\partial u_z}{\partial z} + \frac{\partial \psi_z}{\partial z} \frac{\partial u_x}{\partial x} + \frac{\partial \psi_y}{\partial y} \frac{\partial u_z}{\partial z} \right) \right] dt, \tag{A-6}$$

$$\frac{\partial E_{\mathrm{d}}}{\partial V_{\mathrm{S0}}} = 2\rho V_{\mathrm{S0}} \int_0^T \left[\left(1 + \frac{q}{2} + \frac{1}{2q} \right) \left(\frac{\partial \psi_x}{\partial x} \frac{\partial u_z}{\partial z} + \frac{\partial \psi_z}{\partial z} \frac{\partial u_x}{\partial x} \right) - \left(\frac{\partial \psi_x}{\partial z} + \frac{\partial \psi_z}{\partial x} \right) \left(\frac{\partial u_x}{\partial z} + \frac{\partial u_z}{\partial x} \right) \right] dt, \tag{A-7}$$

$$\frac{\partial E_{\mathrm{d}}}{\partial V_{\mathrm{nmo,P}}} = \frac{-\rho V_{\mathrm{NMO,P}}}{q} \int_0^T \left(\frac{\partial \psi_x}{\partial x} \frac{\partial u_z}{\partial z} + \frac{\partial \psi_z}{\partial z} \frac{\partial u_x}{\partial x} \right) dt, \tag{A-8}$$

$$\frac{\partial E_{\mathrm{d}}}{\partial V_{\mathrm{hor,P}}} = -2\rho V_{\mathrm{hor,P}} \int_0^T \left(\frac{\partial \psi_x}{\partial x} \frac{\partial u_x}{\partial x} \right) dt. \tag{A-9}$$

The gradient for density can be obtained by applying the chain rule to equation A-5:

$$\begin{aligned} \frac{\partial E_{\mathrm{d}}}{\partial \rho} = -\int_0^T \Bigg[& V_{\mathrm{P0}}^2 \left(\frac{\partial u_z}{\partial z} \frac{\partial \psi_z}{\partial z} \right) + V_{\mathrm{hor,P}}^2 \left(\frac{\partial u_x}{\partial x} \frac{\partial \psi_x}{\partial x} \right) \\ & + V_{\mathrm{S0}}^2 \left\{ \left(\frac{\partial \psi_x}{\partial z} + \frac{\partial \psi_z}{\partial x} \right) \left(\frac{\partial u_x}{\partial z} + \frac{\partial u_z}{\partial x} \right) \right\} \\ & + \left(\sqrt{(V_{\mathrm{NMO,P}}^2 - V_{\mathrm{S0}}^2)(V_{\mathrm{P0}}^2 - V_{\mathrm{S0}}^2)} - V_{\mathrm{S0}}^2 \right) \\ & \left(\frac{\partial u_x}{\partial x} \frac{\partial \psi_z}{\partial z} + \frac{\partial u_z}{\partial z} \frac{\partial \psi_x}{\partial x} \right) + v_x \Psi_x + v_y \Psi_y + v_z \Psi_z \Bigg] dt, \end{aligned} \tag{A-10}$$

where

$$q = \sqrt{\frac{V_{\mathrm{nmo,P}}^2 - V_{\mathrm{S0}}^2}{V_{\mathrm{P0}}^2 - V_{\mathrm{S0}}^2}}. \tag{A-11}$$

Here, $\boldsymbol{v}$ and Ψ are the forward- and back-propagated velocity fields, respectively.

REFERENCES

Alkhalifah, T., B. Sun, and Z. Wu, 2018, Full model wavenumber inversion (FMWI): Identifying sources of information for the elusive middle model wavenumbers: Geophysics, **83**, no. 6, R587–R610, doi: 10.1190/geo2017-0775.1.

Asnaashari, A., R. Brossier, S. Garambois, F. Audebert, P. Thore, and J. Virieux, 2013, Regularized seismic full waveform inversion with prior model information: Geophysics, **78**, no. 2, R25–R36. doi: 10.1190/geo2012-0104.1.

Biondi, B., and A. Almomin, 2014, Efficient and robust waveform-inversion workflow: 84th Annual International Meeting, SEG, Expanded Abstracts, 917–921, doi: 10.1190/segam2014-1475.1.

Duan, Y., and P. Sava, 2016, Elastic wavefield tomography with physical model constraints: Geophysics, **81**, no. 6, R447–R456, doi: 10.1190/geo2015-0508.1.

Guitton, A., 2011, A blocky regularization scheme for full waveform inversion: 81st Annual International Meeting, SEG, Expanded Abstracts, 2418–2422, doi: 10.1190/1.3627694.

Guitton, A., G. Ayeni, and E. Daz, 2012, Constrained full-waveform inversion by model reparameterization: Geophysics, **77**, no. 2, R117–R127, doi: 10.1190/geo2011-0196.1.

Hager, W. W., and H. Zhang, 2006, A survey of nonlinear conjugate gradient methods: Pacific Journal of Optimization, **6**, 35–58.

Kamath, N., and I. Tsvankin, 2016, Elastic full-waveform inversion for VTI media: Methodology and sensitivity analysis: Geophysics, **81**, no. 2, C53–C68, doi: 10.1190/geo2014-0586.1.

Kamath, N., I. Tsvankin, and E. Diaz, 2017a, Elastic full-waveform inversion for VTI media: A synthetic parameterization study: Geophysics, **82**, no. 5, C163–C174, doi: 10.1190/geo2016-0375.1.

Kamath, N., I. Tsvankin, and E. Zabihi Naeini, 2017b, Facies-constrained FWI: Toward application to reservoir characterization: The Leading Edge, **36**, 924–930, doi: 10.1190/tle36110924.1.

Kemper, M., and J. Gunning, 2014, Joint impedance and facies inversion-seismic inversion redefined: First Break, **32**, 89–95.

Li, V., A. Guitton, I. Tsvankin, and T. Alkhalifah, 2019a, Image-domain wavefield tomography for VTI media: Geophysics, **84**, no. 2, C119–C128, doi: 10.1190/geo2018-0397.1.

Li, V., I. Tsvankin, A. Guitton, and H. Wang, 2019b, Image-domain wavefield tomography for tilted transversely isotropic media: Geophysical Prospecting, **67**, 2358–2367, doi: 10.1111/1365-2478.12845.

Loris, I., H. Douma, G. Nolet, I. Daubechies, and C. Regone, 2010, Nonlinear regularization techniques for seismic tomography: Journal of Computational Physics, **229**, 890–905, doi: 10.1016/j.jcp.2009.10.020.

Marjanović, M., R.-É Plessix, A. Stopin, and S. C. Singh, 2018, Elastic versus acoustic 3-D full waveform inversion at the east pacific rise 9°50'N: Geophysical Journal International, **216**, 1497–1506, doi: 10.1093/gji/ggy503.

Martin, G., R. Wiley, and K. J. Marfurt, 2006, Marmousi2: An elastic upgrade for Marmousi: The Leading Edge, **25**, 156–166, doi: 10.1190/1.2172306.

Métivier, L., A. Allain, R. Brossier, Q. Mérigot, E. Oudet, and J. Virieux, 2018, Optimal transport for mitigating cycle skipping in full-waveform inversion: A graph-space transform approach: Geophysics **83**, no. 5, R515–R540, doi: 10.1190/geo2017-0807.1.

Operto, S., Y. Gholami, V. Prieux, A. Ribodetti, R. Brossier, L. Metivier, and J. Virieux, 2013, A guided tour of multiparameter full waveform inversion with multicomponent data: From theory to practice: The Leading Edge, **32**, 1040–1054, doi: 10.1190/tle32091040.1.

Pan, W., K. A. Innanen, G. F. Margrave, M. C. Fehler, X. Fang, and J. Li, 2016, Estimation of elastic constants for HTI media using Gauss-Newton and full-Newton multiparameter full-waveform inversion: Geophysics, **81**, no. 5, R275–R291, doi: 10.1190/geo2015-0594.1.

Pan, W., K. A. Innanen, and Y. Wang, 2020, Parameterization analysis and field validation of VTI-elastic full waveform inversion in a walk-away vertical seismic profile configuration: Geophysics, **85**, no. 3, B87–B107, doi: 10.1190/geo2019-0089.1.

Plessix, R.-E., and Q. Cao, 2011, A parametrization study for surface seismic full waveform inversion in an acoustic vertical transversely isotropic medium: Geophysical Journal International, **185**, 539–556, doi: 10.1111/j.1365-246X.2011.04957.x.

Plessix, R.-E., and W. A. Mulder, 2004, Frequency-domain finite-difference amplitude-preserving migration: Geophysical Journal International, **157**, 975–987, doi: 10.1111/j.1365-246X.2004.02282.x.

Singh, S., I. Tsvankin, and E. Zabihi Naeini, 2018, Bayesian framework for elastic full-waveform inversion with facies information: The Leading Edge, **37**, 924–931, doi: 10.1190/tle37120924.1.

Singh, S., I. Tsvankin, and E. Zabihi Naeini, 2019, Bayesian approach to facies-constrained waveform inversion for VTI media: 89th Annual International Meeting, SEG, Expanded Abstracts, 1370–1374, doi: 10.1190/segam2019-3214511.1.

Sun, B., and T. Alkhalifah, 2018, Automatic WEMVA by focusing subsurface offset virtual sources: Geophysics. **83**, no. 2, T49–T68, doi: 10.1190/geo2017-0213.1.
Sun, B., and T. Alkhalifah, 2019, The application of an optimal transport to a preconditioned data matching function for robust waveform inversion: Geophysics, **84**, no. 6, R935–R957, doi: 10.1190/geo2018-0413.1.
Tarantola, A., 1984, Inversion of seismic reflection data in the acoustic approximation: Geophysics, **49**, 1259–1266, doi: 10.1190/1.1441754.
Tikhonov, A., and V. Arsenin, 1977, Solution of ill-posed problems: Winston and Sons, 1–258.
Tsvankin, I., 2012, Seismic signatures and analysis of reflection data in anisotropic media, 3rd ed.: SEG.
Virieux, A., and S. Operto, 2009, An overview of full-waveform inversion in exploration geophysics: Geophysics, **74**, no. 6, WCC1–WCC26, doi: 10.1190/1.3238367.
Wang, H., and I. Tsvankin, 2018, Methodology of waveform inversion for acoustic orthorhombic media: Journal of Seismic Exploration, **27**, 201–226.
Wang, X., and I. Tsvankin, 2013, Multiparameter TTI tomography of P-wave reflection and VSP data: Geophysics, **78**, no. 5, WC51–WC63, doi: 10.1190/geo2012-0394.1.
Warner, M., A. Ratcliffe, T. Nangoo, J. Morgan, A. Umpleby, N. Shah, V. Vinje, I. Å tekl, L. Guasch, C. Win, G. Conroy, and A. Bertrand, 2013, Anisotropic 3D full-waveform inversion: Geophysics, **78**, no. 2, R59–R80, doi: 10.1190/geo2012-0338.1.
Wu, Z., and T. Alkhalifah, 2016, Waveform inversion for acoustic VTI media in frequency domain: 86th Annual International Meeting, SEG, Expanded Abstracts, 1184–1189, doi: 10.1190/segam2016-13867221.1.
Xu, S., D. Wang, F. Chen, Y. Zhang, and G. Lambare, 2012, Full waveform inversion for reflected seismic data: 74th Annual International Conference and Exhibition, EAGE, Extended Abstracts, doi: 10.3997/2214-4609.20148725.
Zabihi Naeini, E., and R. Exley, 2017, Quantitative interpretation using facies-based seismic inversion: Interpretation, **5**, no. 3, SL1–SL8, doi: 10.1190/INT-2016-0178.1.
Zabihi Naeini, E., and D. Hale, 2015, Image- and horizon-guided interpolation: Geophysics, **80**, no. 3, V47–V56, doi: 10.1190/geo2014-0279.1.
Zhang, Z., T. Alkhalifah, and E. Zabihi Naeini, 2017, Multiparameter elastic full waveform Inversion with facies constraints: 87th Annual International Meeting, SEG, Expanded Abstracts, 1551–1555, doi: 10.1190/segam2017-17672943.1
Zhang, Z., T. Alkhalifah, E. Zabihi Naeini, and B. Sun, 2018, Multiparameter elastic full waveform inversion with facies-based constraints: Geophysical Journal International, **213**, 2112–2127, doi: 10.1093/gji/ggy113.